Research Article Vol. 57, No. 26 / 10 September 2018 / Applied Optics 7501

applied optics

Energy calibration of integrated path differential absorption lidars

Andreas Fix,* Mathieu Quatrevalet, Axel Amediek, and Martin Wirth

Deutsches Zentrum für Luft- und Raumfahrt (DLR), Institut für Physik der Atmosphäre, 82234 Oberpfaffenhofen, Germany
**Corresponding author: Andreas.Fix@dlr.de*

Received 26 June 2018; revised 7 August 2018; accepted 7 August 2018; posted 8 August 2018 (Doc. ID 336162); published 7 September 2018

The stringent requirements for energy reference measurement represent a challenging task for integrated path differential absorption lidars to measure greenhouse gas columns from satellite or aircraft. The coherence of the lidar transmitter gives rise to speckle effects that have to be considered for accurate monitoring of the energy ratio of outgoing on- and off-line pulses. Detailed investigations have been performed on various measurement concepts potentially suited for deployment within future satellite missions.

OCIS codes: (010.3640) Lidar; (280.1910) DIAL, differential absorption lidar; (120.5630) Radiometry; (030.6140) Speckle; (120.3150) Integrating spheres; (040.5160) Photodetectors.

https://doi.org/10.1364/AO.57.007501

1. INTRODUCTION

Accurate energy measurements of individual laser pulses are important for a variety of applications, such as in laser marking processes, micromachining, laser micro-surgery, and, in particular, for lidar.

In the scope of this work, energy calibration of integrated path differential absorption lidar (IPDA) measurements is discussed. This active remote sensing technique, using hard-target reflection from lasers in the near-infrared spectral range, has the potential to deliver atmospheric trace gas columns, and in particular those of the most important anthropogenic greenhouse gases (GHGs), carbon dioxide (CO_2) and methane (CH_4), from satellite and aircraft with unprecedented accuracy [1]. Since the pre-industrial age until today (2015), the average atmospheric mole fractions of CO_2 and CH_4 have increased due to human activities by as much as 44% (from ~278 ppm to 400 ppm) and 156% (from ~700 ppb to 1845 ppb), respectively, and accounted for about 65% and 17% of total increase in the radiative forcing due to long-lived GHGs in the atmosphere [2]. It is generally accepted that there is an urgent need to accurately measure these important GHGs on all relevant temporal and spatial scales in order to better than today quantify carbon fluxes, assess the effectiveness of emission reduction schemes (e.g., Paris Agreement, COP21), and predict the rate of climate change on our planet throughout the 21st century.

In order to address these needs, a variety of research centers and space agencies around the world investigate and develop spaceborne IPDA systems and airborne demonstrators, respectively, e.g., Refs. [3–15]. An example is A-SCOPE (Advanced Space Carbon and Climate Observation of Planet Earth), which was investigated by ESA as a prephase-A Earth Explorer Mission [16]. Comprising a nadir-viewing CO_2 lidar instrument as the core element, A-SCOPE did not yet advance for later phases due to lacking technology readiness. NASA is pursuing a similar concept with ASCENDS (Active Sensing of CO2 Emissions over Nights, Days, and Seasons) [17]. The IPDA technique will also be employed by the German–French climate mission MERLIN (Methane Remote Sensing LIDAR Mission) but for methane as the target greenhouse gas [18]. The MERLIN mission will be the first trace gas lidar in orbit and is scheduled for launch in the 2023 time frame. For the preparation of MERLIN, future validation activities and scientific deployments, an airborne demonstrator (CHARM-F) has been developed at German Aerospace Center (DLR) [15].

Within the technology studies for A-SCOPE and MERLIN as well as the development of CHARM-F, detailed investigations on the energy calibration issue have been performed, which are generally applicable to IPDAs but whose results have a significant impact for the current design of CHARM-F and MERLIN.

IPDA uses the laser light scattered back from a surface ("hard target") to obtain measurements of the column content of a specific atmospheric trace gas between lidar and target, which typically constitutes the Earth's surface or clouds. Figure 1 shows the measurement geometry of a nadir-viewing lidar with the measurements aligned along the sub-satellite or aircraft track. Differential absorption uses the difference in atmospheric transmission between a wavelength tuned onto or near the center of an absorption line, denoted on-line, and a reference off-line wavelength with significantly less absorption. Close collocation of the on- and off-line wavelength positions is required to avoid biases by the wavelength dependency of aerosols, clouds, and the

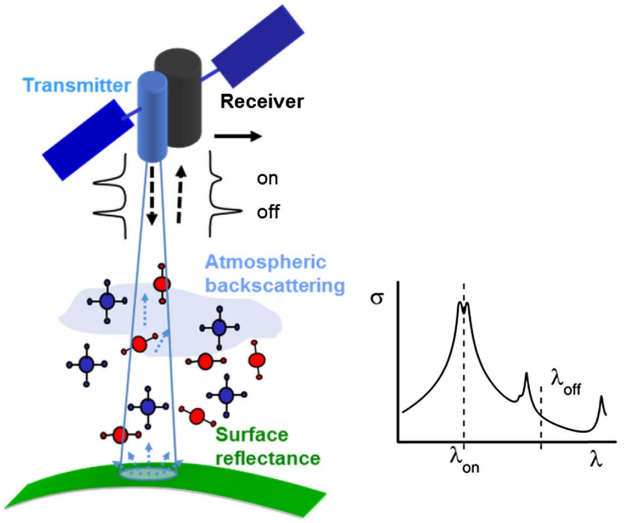

Fig. 1. Schematic setup of a space-based integral path differential absorption lidar.

surface. In addition, close spatial beam collocation of on- and off-line beams is mandatory to circumvent biases by the variability of atmospheric and surface scatter. IPDA largely eliminates the contribution of atmospheric scattering by particles and clouds, which greatly affects the achievable accuracy of passive remote sensing instruments. Moreover, this technique can be applied during daytime or night-time and at all latitudes since—in contrast to many passive remote sensing techniques—it does not depend on solar radiation. However, the necessity imposed by scientific needs to accurately infer GHG fluxes demands very stringent requirements of the system parameters and in particular for precise measurement of the ratio of outgoing on- and off-line pulses. Errors in the determination of this quantity directly result in errors in the IPDA measurement.

2. REQUIREMENTS

A. Definition of Requirements

The quantity of scientific interest is the weighted average of the GHGs' dry-air volume mixing ratio along the probed column, XGHG (e.g., XCO_2 or XCH_4), which is given by Ref. [1]:

$$\mathrm{XGHG} = \frac{\frac{1}{2}\cdot \ln\left(\frac{P_{\mathrm{off}}\cdot E_{\mathrm{on}}}{P_{\mathrm{on}}\cdot E_{\mathrm{off}}}\right)}{\int_{p=0}^{p_{\mathrm{SFC}}} \mathrm{WF}_{\mathrm{GHG}}(p)\cdot \mathrm{d}p} = \frac{\mathrm{DAOD}}{\mathrm{IWF}}. \tag{1}$$

The denominator in Eq. (1) is the integral of the so-called weighting function (IWF) along the probed column down to surface pressure (p_{SFC}), determined solely by the temperature and pressure-dependent differential absorption cross section for the considered wavelengths and atmospheric parameters, such as air density and humidity that can be obtained from the numerical weather prediction (NWP) model results. The numerator is the differential atmospheric optical depth (DAOD) where Pon/off and Eon/off are the measured ground echoes and outgoing pulse energies at the corresponding wavelengths, respectively. Then, assuming that the uncertainties add in quadrature, the total relative uncertainty on the column content XGHG is given by differentiating Eq. (1):

$$\frac{\delta \mathrm{XGHG}}{\mathrm{XGHG}} = \sqrt{\frac{1}{\mathrm{DAOD}^2}\sum_i \left(\frac{\partial \mathrm{DAOD}}{\partial \nu_i}\delta\nu_i\right)^2 + \frac{1}{\mathrm{IWF}^2}\sum_i \left(\frac{\partial \mathrm{IWF}}{\partial \nu_i}\delta\nu_i\right)^2}. \tag{2}$$

Here, ν_i are all variables that are potentially prone to systematic errors, and $\delta\nu_i$ are the associated systematic error magnitudes. Systematic errors can arise from a laser transmitter or receiver errors (e.g., spectral errors induced by unknown laser wavelength instability, laser bandwidth uncertainties, uncertainties in the measurements of the ratio of the on-/off-line pulse energies, detector nonlinearity, etc.), atmospheric uncertainties (e.g., temperature, pressure, and humidity), from uncertainties in the spectroscopic database, or from geometric uncertainties (e.g., misalignment between laser and telescope, or unknown Doppler shift due to unidentified mispointing). In the context of this work, the focus is on uncertainties in the measurement of the ratio of the on-/off-line pulse energies.

In preparation of the A-SCOPE mission, a number of feasibility studies have been undertaken [1,19,20]. The target and threshold mission requirements for the accuracy of the primary data product XCO_2 have been set to 0.05 ppm and 0.15 ppm, respectively, for an observation averaged over 50 km along the satellite track. These figures apply to non-random residual errors that remain after correction for any known source of systematic error [16]. For the random error, the allowed target and threshold values are a factor of 10 higher, thus 0.5 ppm and 1.5 ppm, respectively. Using inverse modeling, such error margins would allow for constraining the CO_2 fluxes to within 0.02 $\mathrm{Pg/Cyr^{-1}}$ on a scale of 1000 km × 1000 km [16].

A similar definition of user requirements has been performed for MERLIN [18]. In order to provide global measurements of the spatial and temporal gradients of atmospheric CH_4 with a precision and accuracy sufficient to significantly constrain methane surface fluxes, the target and threshold requirements for the XCH_4 systematic error have been set to 1 ppb and 3 ppb, respectively, for an observation averaged over 50 km along the satellite track. The accepted target and threshold values for the random error are 8 ppb and 36 ppb, respectively. The very low levels of systematic error aim at avoiding geographical biases (geographical and temporal) in the XGHG fields that could lead to uncertainties in flux estimation.

B. Allan Variance Concept

The concepts of "random error" and "systematic error" may be interpreted in terms of uncorrelated (stochastic) and correlated (deterministic) measurement noise, respectively. However, there is an infinite continuum of possible correlations at any timescale in a noisy time series, from fully uncorrelated noise, commonly referred to as white noise, to fully correlated "noise" such as an unknown linear drift. A powerful mathematical tool to identify and quantify these different types of noises is the Allan variance. A preferred implementation of the latter is the so-called overlapping Allan variance, because it makes use of all the information contained in a given time series y_i of M measurements of a random variable y with even temporal sampling τ_0 [21]:

$$\sigma_y^2(m\cdot\tau_0)=\frac{1}{2\cdot m^2(M-2m+1)}\sum_{j=1}^{M-2m+1}\left\{\sum_{i=j}^{j+m-1}[y_{i+m}-y_i]\right\}^2, \quad (3)$$

where $m\cdot\tau_0$ is the so-called averaging time. The Allan variance (or its square root, the Allan deviation) may be considered to quantify the effect of a gliding average on the magnitude of the noise on y. This is best visualized on a log-sigma versus log-tau plot, such as the one in Fig. 2. If the noise is uncorrelated i.e., purely white, its magnitude decreases with averaging time following a –0.5 slope ($\tau^{-1/2}$). If correlated noise is present, the decrease may be less steep, and if $1/f$ noise is present, a "noise floor" will be reached after a certain timescale: further averaging of the data does not reduce the magnitude of the noise because ever stronger low-frequency correlated noise components compensate the reduction of the contribution from higher-frequency noise. For Brownian noise with a $1/f^2$ power spectral density, they outweigh it and the magnitude of the noise actually increases with averaging time [21].

C. Allan Templates for the A-SCOPE and MERLIN Requirements

The above considerations may be applied to the requirements of IPDA measurements where y is XGHG. The solid and dot-dashed lines, respectively, in Fig. 2 have been computed as the geometrical sum of the ideal Allan deviation of pure white noise with a magnitude, such that it reaches the values for the threshold and target *random* error levels for the A-SCOPE and MERLIN requirements at an averaging time of 7 s (corresponding to 50 km averaging for a satellite orbiting at 7 km/s), and $1/f$ noise with a magnitude corresponding to the *systematic* error requirements. A "continuous" and more rigorous reformulation of the A-SCOPE and MERLIN requirements is for the Allan deviation of the measurement noise to lie under the threshold curve and preferably under the target curves in Fig. 2. This reflects the fact that the random error requirement applies to the magnitude of uncorrelated noise at short averaging times, while the systematic error requirement puts an upper limit on the magnitude of correlated errors at "long" timescales up to the satellite lifetime.

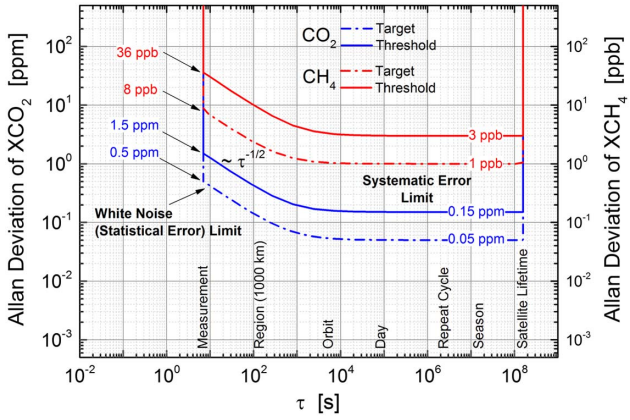

Fig. 2. Template expressing the A-SCOPE (XCO_2) and MERLIN (XCH_4) random and systematic error requirements in terms of Allan deviation.

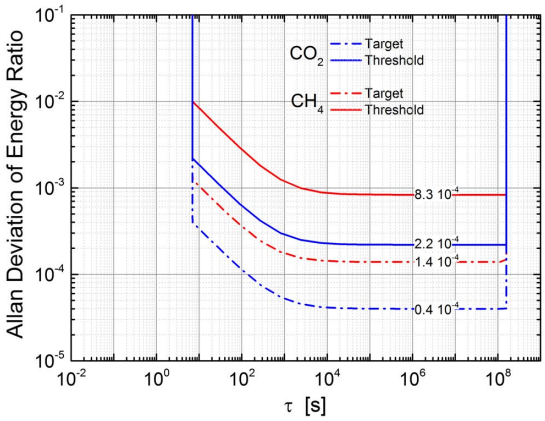

Fig. 3. Template expressing the requirements for the energy ratio measurement in terms of the Allan variation for A-SCOPE (XCO_2) at a wavelength of 1.57 μm and MERLIN (XCH_4) at 1.64 μm, respectively.

From this template, the requirements for the energy ratio (E_{on}/E_{off}) were derived using Eq. (2) under the assumption that for the threshold (target) case, the individual contribution must not exceed 50% (25%) of the total error budget. The corresponding results are depicted in Fig. 3. It has to be noted that for the CO_2 IPDA (A-SCOPE type), measurement wavelengths in the 1.57-μm band have been assumed. This wavelength set leads to more stringent requirements than an alternative wavelength set identified at 2.05 μm [16]. However, the preferred wavelength range remains under discussion, since better detectors at shorter wavelengths counterbalance the error budget. For the CH4 IPDA, indisputably, wavelengths at 1.64 μm are the preferred choice [1].

As a consequence, these requirements serve as the benchmark for the following breadboard study.

D. Detector Issues

From the above given argumentation, accurate IPDA measurements of GHGs ask for an accuracy of the measurement of the ratio of outgoing on- and off-line pulse energies of the order of one part to the 10^4.

In order to measure energy or power of pulsed laser sources, three different technologies can be taken into account:

- calorimetry,
- pyroelectric detectors, or
- optical semiconductors.

In calorimetric detectors, energy is converted into heat at an absorber, and the resulting temperature rise is measured with a thermal sensor, e.g., Ref. [22]. As a consequence, these types of detectors are slow; therefore, it is not possible at all to distinguish the energies of individual pulses in a pulse train, which is required for IPDA where subsequent pulses of on-line and off-line radiation have to be registered for ratioing. Therefore, only pyroelectric detectors or photodiodes are left over.

Pyroelectric detectors show advantages in linearity, sensitivity over a very large spectral bandwidth, low temperature dependence, and low power requirements [23].

In general, power and energy meters are calibrated against standards that are operated at national metrology institutes and

that typically are based on calorimetric sensors [24]. Energy calibrations are essentially the same as power calibrations, except that the period during which the power is applied is also measured.

Their performance is primarily limited by inequivalence between electrical and optical heating, due to factors such as radiative and convective cooling of the optical receiver, and its limited diffusivity, which results in the formation of temperature gradients, and parasitic heating in the electrical heater leads [24]. Best performance can be achieved using calibrated cryogenic radiometers operating near liquid helium temperatures, which usually serve as the primary standards [25] and which nowadays provide uncertainties of less than a few parts in 10^4. Non-cryogenic, portable power, and energy transfer standards hardly achieve accuracies below 1% [25–27].

Therefore, achieving pulse energy accuracies on the order of 10^{-4} is difficult. However, this requirement is alleviated by the fact that for IPDA, only pulse energy *ratios* have to be accurately known rather than absolute energies. But, in order to do so, it has to be assured that neither effects of beam steering, different beam profiles, nor ageing effects (influencing the spectral response of the detector in a different way for on- and off-line pulses) will lead to systematic errors of the energy calibration.

In the past, IPDA applications have used either separate pyroelectric detectors [28–30] or photodiodes to normalize the pulse intensities [31]. Also, in more recent developments, separate photodetectors are usually used as the transmitter monitor [4,6,32]. In order to avoid beam steering and profile effects, the use of integrating spheres seems favorable, since their transmission does not depend on spatial effects. This was realized, e.g., by Refaat *et al.* [33] and Numata *et al.* [34].

For the first time, Amediek *et al.* [3] used the same (photodiode) detector for the acquisition of both the energy calibration signals and the ground or cloud echoes to avoid variations in the optical-to-electrical response that may occur in the case of two completely separate detection chains, such as different evolutions of the spectral responses of the detectors from ageing, or the pointing-dependent spectral transmission of coatings or interference filters in front of the detectors. Such a concept, which requires attenuation factors of about 11 to 14 orders of magnitude (depending on the geometry) along the energy calibration path to match the magnitude of the return signals, was also proposed for the A-SCOPE mission [16]. Quatrevalet *et al.* [35] later also realized this approach by using an integrating sphere as well as the same detector. A similar design that will be discussed in more detail below is implemented in the CHARM-F airborne GHG lidar [15]. This concept, however, requires a careful investigation of the magnitude, spectral, and spatial effects of the attenuation as well as the consideration of speckle effects. This is treated in detail in the following section.

3. INTEGRATING SPHERES

A. Attenuation of Single- and Dual-Integrating Spheres

One of the standard materials of integrating spheres is Spectralon. Spectralon is a sintered fluoropolymer (polytetrafluoroethylene, PTFE) that can be machined into a wide variety of shapes for the construction of optical components. It has the highest diffuse reflectance of any known material or coating over the ultraviolet, visible, and near-infrared regions of the spectrum [36]. It exhibits highly Lambertian behavior, is usable from ~250 nm to 2500 nm, and was space qualified for a number of applications (e.g., Ref. [37]). An estimate of the throughput of a sphere to a detector has, e.g., been derived in Ref. [36]:

$$\eta_d = \frac{1}{\pi \cdot A_s} \cdot \frac{\rho}{1 - \rho \cdot (1 - f)} \cdot A_d \cdot \Omega, \tag{4}$$

where ρ is the sphere's reflectance, A_s is the sphere surface area, f is the port fraction, Ω is the solid angle subtended by the detector at the port, and A_d is the active area of the detector.

When a fiber is used to collect the light at a given port, we have to account for the solid angle Ω defined by the numerical aperture (NA) of the fiber, the reflectivity r_f of the fiber facet, and the effective core area of the fiber end, A_f:

$$\eta_f = \frac{1}{\pi \cdot A_s} \cdot \frac{\rho}{1 - \rho \cdot (1 - f)} \cdot A_f \cdot (1 - r_f) \cdot \pi \cdot (\mathrm{NA})^2. \tag{5}$$

Therefore, the attenuation can be varied to a great degree with the multimode fiber (MMF) core diameter and to some extent with the NA of the fiber and the size of the sphere. As an example, the attenuation using a 3.3"-diameter sphere, with wall reflectivity of 97%, coupled to a fiber with a core diameter of 200 μm and a NA of 0.39 yields an attenuation of $\sim 2.5 \cdot 10^{-7}$. Further attenuation can be achieved using a double-integrating sphere setup, as depicted in Fig. 4. A theory of the throughput of two integrating spheres that are separated by a semi-transparent diffusor with area Φ_D and transmission T_D has been derived in the context of biological tissue analysis [38]. Here, we follow this approach to derive the transmission of such a system as depicted in Fig. 4. For simplicity, we require the sphere reflectance ρ to be identical for both spheres and assume no absorption within the diffusor. However, we allow the sphere surface areas of the two spheres, A_{S1} and A_{S1}, and their port fractions, f_1 and f_2, to be different. It is assumed that two detectors with apertures A_{d1} and A_{d2} and surface reflectivities r_1 and r_2 are attached to the respective sphere.

In this case, signal ratio of detector #2 to detector #1 (assumed identical) is

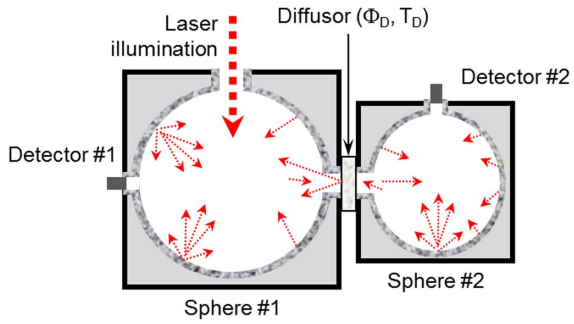

Fig. 4. Schematic setup of a double sphere consisting of two spheres with different diameters separated by a diffusor with aperture Φ_D and transmission T_D.

$$\frac{\eta_{d2}}{\eta_{d1}} = \frac{A_{d2}}{A_{d1}} \cdot \frac{A_{S1}}{A_{S2}} \cdot \frac{V_1}{V_2} \cdot \left(\frac{\Phi_D \cdot T_D}{A_{S1} \cdot V_1}\right). \quad (6)$$

$V_{1,2}$ are given by the following expression:

$$V_{1,2} = 1 - \left[\rho \cdot f_{1,2} + (1 - T_D) \cdot \frac{\Phi_D}{A_{1,2}} + r_{1,2} \cdot \frac{\delta_{1,2}}{A_{1,2}}\right]. \quad (7)$$

Therefore, by choosing an appropriate diameter of the hole between the spheres and transmission of the diffusor, the attenuation can gradually be increased independent of beam profile, polarization, and wavelength or pick-up fiber. In an experimental verification, a reasonably good agreement of Eq. (7) with measured data could be achieved given the known accuracies of the input parameters.

For example, a second sphere of diameter 1.5", respectively, a hole with 5 mm diameter, and a diffusor sheet with a transmission of 33%, the attenuation can further be reduced by two orders of magnitude versus the single-sphere system.

Together with the attenuation factor of the pick-up system (see Section 6.A), the mere attenuation required for the energy reference to roughly match with the received lidar signal does not appear to be a problem.

B. Speckle Statistics

Speckles appear in a signal when that signal is composed of a multitude of independently phased, additive complex components. Integrating spheres are known to generate an ideal (Gaussian) speckle pattern [39]. When detecting speckle patterns, it is distinguished between objective and subjective speckles. An "objective speckle pattern" is created when laser light that has been scattered off a rough surface falls on another surface (Fraunhofer plane). When a speckle pattern is imaged using an optical system, a "subjective speckle pattern" is created in the image plane (Fig. 5). For the case considered here, we deal with an objective speckle pattern that is captured by either a pyroelectric detector or a fiber.

The approximate speckle size of objective speckles ε_o (Fig. 5) is given by the Fraunhofer diffraction pattern of a circular aperture and corresponds to the size of the Airy disc (e.g., Refs. [40,41]):

$$\varepsilon_o \approx 1.22 \cdot \frac{\lambda \cdot z}{D}. \quad (8)$$

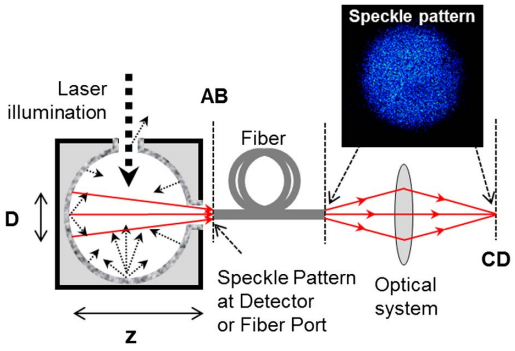

Fig. 5. Illustration of the formation of speckle at the exit of an integrating sphere and a pick-up fiber, respectively. D, area subtended; Z, distance to observation plane AB; CD, plane of the imaged fiber end. Note that each speckle pattern is different.

The scattered field amplitudes are randomly distributed, and the intensity follows a negative exponential distribution (e.g., Ref. [42]):

$$P(I) = \frac{1}{\langle I \rangle} \cdot e^{-\frac{I}{\langle I \rangle}}. \quad (9)$$

When complete depolarization of the reflected wave occurs, which is the case for an integrating sphere [43], the two (parallel and perpendicular) speckle fields incoherently combine, and when all $\langle I_n \rangle$ are identical and equal to $\langle I \rangle$, the probability distribution function is a gamma distribution of order 2 (e.g., Ref. [42]):

$$P(I) = \frac{4I}{\langle I \rangle^2} \cdot e^{-2\frac{I}{\langle I \rangle}}. \quad (10)$$

In this case, the contrast of the total speckle pattern is $1/\sqrt{2}$, rather than unity.

The level of speckle-related relative intensity noise thus is expected to be $1/\sqrt{2N}$, where N is the number of speckles. The level of speckle intensity noise on a detector of size $d \times d$ is related to the number of speckles N and thus speckle size. The number of speckles is approximately d^2/ε_o^2. It follows that the intensity related noise is

$$\frac{\Delta I}{I} \approx \frac{1.22}{\sqrt{2}} \cdot \lambda \frac{z}{D \cdot d}. \quad (11)$$

When using a pick-up fiber, the speckle size can be expressed as a function of NA of the fiber:

$$\varepsilon_0 \approx 1.22 \cdot \lambda \frac{1}{\tan(\sin^{-1}\mathrm{NA})} \approx 1.22 \cdot \frac{\lambda}{\mathrm{NA}}. \quad (12)$$

Assuming that the detector does not truncate the fiber output, the respective speckle-related intensity noise at the end of a MMF thus is approximately

$$\frac{\Delta I}{I} \approx \frac{\lambda}{a} \cdot \frac{1}{\mathrm{NA}}, \quad (13)$$

where a is the core diameter of the fiber.

For completeness, the size of the subjective speckles ε_s for an imaging system with f-number $f/\#$ is given by, e.g., Ref. [40], which supposes that the optical system images the speckle surface:

$$\varepsilon_s \approx 1.22 \cdot \lambda(1 + M) f/\#, \quad (14)$$

where M is the magnification of the optical system.

For some of the MMFs used in the experiments that will be described below, the expected speckle-related intensity noise at the fiber end is listed in Table 1.

4. TEST BED DESIGN

A. Laser Source

In order to investigate possible monitoring concepts, a pulsed-laser test bed was used based on an optical parametric oscillator (OPO) (Fig. 6). This OPO test bed was devised as an engineering bread board for CHARM-F, as well as to support A-SCOPE-related technology investigations [44].

The OPO uses potassium titanyl arsenate (KTA) as the nonlinear optical material and is pumped by an injection-seeded, diode-pumped Nd:YAG laser [44].

Table 1. Calculated Speckle Noise According to Eq. (13) for a Wavelength of 1572 nm for Some of the MM Fibers Used Within this Study

Fiber	Core Diameter (μm)	N.A.	Speckle Noise (%)
FT400 EMT (Thorlabs)	400	0.39	1.0
FT300 EMT (Thorlabs)	300	0.39	1.3
FT200 EMT (Thorlabs)	200	0.39	2.0
FG105 LCA (Thorlabs)	105	0.22	6.8
IG 50/125/2 (*j*-fiber)	50	0.22	14

This laser can be operated in double-pulse mode, thereby emitting two pulses with a separation of ~360 μs at a 50-Hz rate, or at 100 Hz single pulse. Narrowband operation of this laser is realized by means of injection seeding using a distributed feedback (DFB) fiber laser at 1064 nm and a pulse build-up-time (BUT) stabilization technique. Narrowband operation of the OPO is likewise achieved by injection seeding using two DFB lasers operating around 1572 nm. By means of a fast fiber switch, the seed wavelength can be altered from pulse to pulse (Fig. 6). The piezo-controlled cavity length of the OPO is matched to the seed wavelength using a heterodyne stabilization technique [44]. Since an independent control for on-line and off-line stabilization would result in high dynamic load on the piezoelectric transducer (PZT), an alternative control was used (Fig. 7) for double-pulse operation: the OPO cavity is matched to the on-line seed wavelength, whereas the off-line laser is tuned onto a nearby cavity mode of the OPO [separated by an integral multiple of the cavity free spectral range (FSR)] using a digital feedback loop controlling the wavelength of the DFB laser. This method is also used for CHARM-F [15] and will be implemented for MERLIN.

For the validity of the experiments described below, the wavelength is of minor relevance, and in some of the cases, where dual-wavelength operation was not required, the 1064-nm Nd:YAG laser radiation was used within the energy-monitoring experiments. This somewhat simplified the experiments that mostly required many hours of data

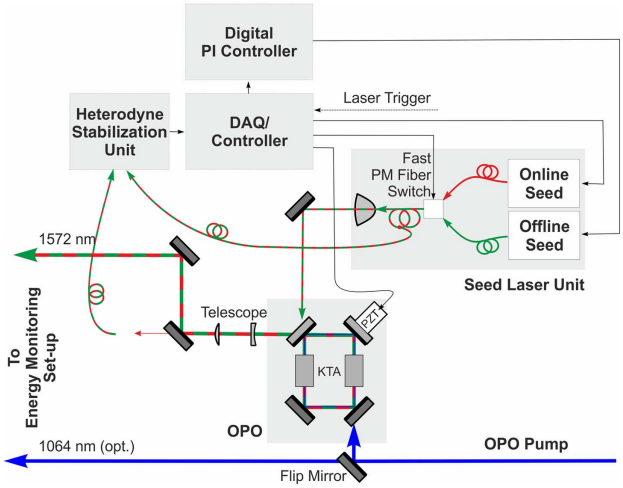

Fig. 6. Setup of the optical parametric oscillator.

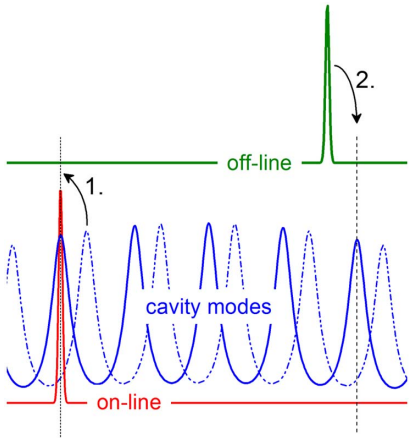

Fig. 7. Schematic of the method to stabilize the OPO cavity to the on-line laser and the off-line to the OPO. The OPO cavity modes are first matched to the on-line seed wavelength. Subsequently, the off-line seed is controlled to be coincident with a stabilized OPO cavity mode separated by an integral multiple of its FSR.

recording. For that purpose, a flip mirror transmitted the Nd:YAG laser beam to the respective experiment (Fig. 6). Also, the Nd:YAG laser could be operated in non-seeded, broadband mode to investigate effects of reduced coherence. Since the detectors used were by far sensitive enough, the pump laser and OPO were operated at reasonably low energies and in most cases had to be further reduced by means of filters or reflecting surfaces to a level that guarantees no saturation.

B. Detection Schemes

One of the main challenges when determining the accuracy of the energy ratio measurement is the lack of a reference system that may serve to provide the "true" value against which the experimental setup [device under test (DUT)] can be referenced. Therefore the energy ratios had to be simultaneously measured twice using the same or a different measurement technique and analyzed using statistical methods. Again, the Allan variance is used to identify uncorrelated and correlated measurement noise. In general, the different setups investigated use two detectors (see Table 2 for a list of used detectors) to monitor the pulse energies. Usually, but not exclusively, the detectors are of the same type and arbitrarily dubbed D1 and D2, respectively. As an example, the two detectors can be attached to two ports of the same integrating sphere but may also be attached to different spheres.

The pulses of the first two detector types in Table 2 were recorded with a two-channel, 12-bit high-speed digitizer (Acqiris DC440) with a time resolution of 2.5 ns using an acquisition program written in LabVIEW. The relative energies

Table 2. List of Detectors

Detector	Type	Manufacturer	Diameter [mm]
InGaAs PIN	PDA20CS	Thorlabs	2.0
Pyroelectric	PEM12E	SLR GmbH	12.0
Pyroelectric	*J*-10 MT-10 KHZ	Coherent	10.5

of each individual pulse were calculated from typically six values around the peak. The Coherent detectors come with their own data acquisition and analysis software to measure the time series of pulse energies. Synchronized recording of two detector readings (and their ratio) can be performed when one detector acts as the master, which can externally be triggered.

C. Data Analysis

For each of the two detectors D1 and D2, the time series of the reading of each individual laser pulse $E_{1,n}$ and $E_{2,n}$ (where n is the pulse number) is recorded together with their ratio R_n:

$$R_n = E_{1,n}/E_{2,n}. \tag{15}$$

Furthermore, we calculate a quantity that we name "double ratio (DR)" which is calculated from two subsequent pulses recoded by the two detectors according to the ratios of the detector readings of both detectors:

$$\mathrm{DR}_i = R_{2n-1}/R_{2n} = \left(\frac{E_{1,2n-1}}{E_{2,2n-1}}\right) \cdot \left(\frac{E_{2,2n}}{E_{1,2n}}\right), \qquad i = n/2. \tag{16}$$

The mean value of the DR should ideally be unity. By means of this definition, we mimic the energy ratio of on-line and off-line wavelengths that are alternatively changed even if our measurement is performed using a single wavelength only. In single-pulse operation (100 Hz), the second pulse arrives 10 ms after the first pulse, whereas in double pulse operation (50 Hz), this separation is on the order of 360 µs.

Finally, the (overlapping) Allan variance is applied to the readings of the individual detectors, the single ratio, and the DR. In general, the DR shall meet the requirements given in Section 2, but it is nevertheless helpful to display the Allan variances of the other quantities as well, as this helps to track drift mechanisms and periodicities.

5. LAB RESULTS

The most important finding of the investigations was the corroboration that speckles and the partial correlation of their patterns can cause a significant deviation from the requirements defined in Section 2. As an example, Fig. 8 shows the time series of the individual pulse energies recorded by two InGaAs positive intrinsic negative (PIN) photodiodes, which were fiber coupled to two individual integrating spheres (diameter 3.3") using MMFs with a core diameter of 105 µm and a length of 2 m.

The green and blue curves are the on-line (first) and off-line (second) pulse energies measured at the first sphere, and the black and red curves show the same, but for the second sphere, which receives less pulse energy. Also the offline pulse is slightly more energetic than the online one. It is immediately obvious that although its mean value is ~1, the behavior of DR deviates significantly from white noise. This is quantitatively supported by the evaluation of the Allan deviation shown in Fig. 9. In this figure, the Allan deviation of DR for that case is given by the red squares and, clearly, the curve does not follow a –0.5 slope and shows a maximum at a time scale of ~100 s.

In subsequent investigations, it was revealed that these effects are much more pronounced in the double-pulse,

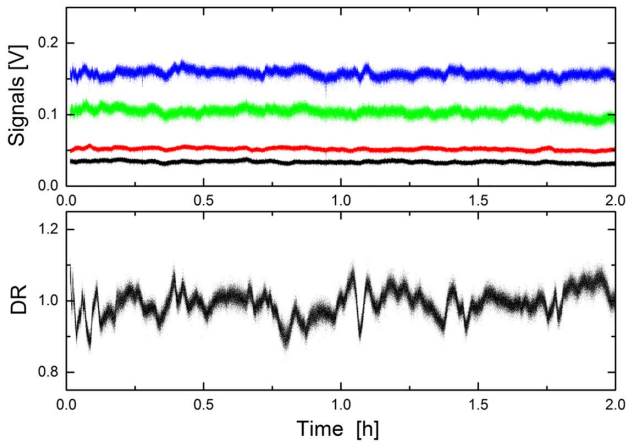

Fig. 8. Time series of the individual detector signals (top) and the respective DR [according to Eq. (16), bottom] over 2 h of operation (= 720.000 individual pulses). The InGaAs photodiodes were fiber coupled using multimode fibers with a core diameter of 105 µm.

dual-wavelength operation than in single-wavelength or single-pulse mode. This finding is shown in Fig. 9. While the Allan deviation of the energy ratio of single pulses with a separation time of 10 ms results in an almost ideal –0.5 slope (and would easily meet the threshold requirements), this is not true for the double-pulse mode. Since the noise is reduced with the number of speckles captured, the effect is more prominent for a smaller (105-µm) fiber (cmp. Table 1). It proved to be irrelevant whether the detectors were attached to two different spheres or to two different ports of the same one.

Thus, the temporal change of speckle patterns between double pulse sequences is too large to maintain full correlation but too short to entirely destroy their correlation. For single pulses, separated by 10 ms, this correlation appears to be fully

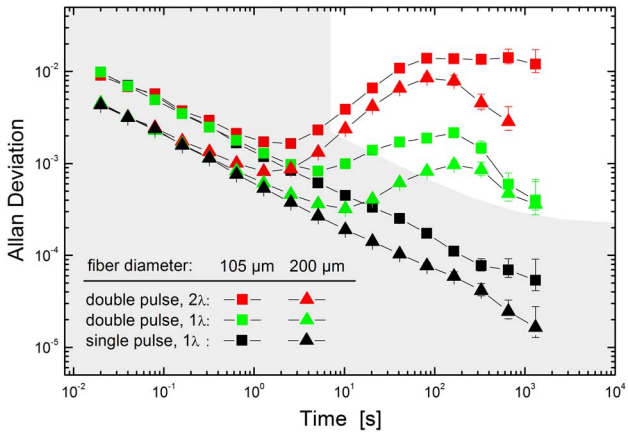

Fig. 9. Allan deviations of the DR of two subsequent pulses at 1.57 µm recorded with two fiber-coupled PIN detectors with a fiber diameter of 105 µm (squares) and 200 µm (triangles), respectively. The nominal on-line/off-line double-pulse sequence is given in red. Green symbols designate the double-pulse mode but no switching of wavelengths, whereas the result for a single-pulse (100 Hz) sequence is given in black. In order to gauge these results, the shaded area depicts the range that has to be met for the A-SCOPE threshold requirements.

destroyed. Also, the deviation of the effective surface height fluctuations $\Delta\sigma_h$, which is required to be on the order of

$$\Delta\sigma_h \approx \frac{c}{2 \cdot \Delta\nu} \tag{17}$$

to produce uncorrelated speckle [45,46] due to wavelength decorrelation, is obviously too small for the difference between on- and off-line frequency. Here, a $\Delta\sigma_h$ of a few millimeters would be required.

For pyroelectric detectors with their large aperture, the speckle noise is expected [see Eq. (11)] to be much less pronounced. Therefore, the experiment was repeated with pyroelectric detectors instead of fiber-coupled photodiodes. Those results are given in Fig. 10. All results, double-pulse dual as well as single-wavelength operation, and single-pulse single-wavelength operation are close to white noise and even for the nominal operation (double-pulse, dual-wavelength) would meet the A-SCOPE *target* requirements.

According to Eq. (11), the speckle noise for a 3.3-inch sphere and an aperture of 10.5 mm of the detector is estimated to be on the order of 10^{-4}, and, indeed, the deviations from the −0.5 line appear at noise levels below 10^{-4}. In another experiment, not shown here, using a sphere port that partly obstructed the sensitive area of the pyroelectric detectors, thus reducing the effective speckle number, the deviations from the white-noise behavior appeared at higher noise levels.

As an intermediate conclusion, it turns out that, by increasing the number of speckles using large-area detectors, the unwanted noise is significantly reduced, at least for the time scales investigated. By means of a ∼10 mm detector the noise scaled down, such that even the extremely stringent A-SCOPE requirements were fulfilled. For this, the detectors have to be fast enough to temporally separate the individual pulses of the double-pulse sequence, which favors pyroelectric detectors.

However, this scheme would require deviating from the concept of measuring the return pulses and outgoing pulse energy with the same detector. Thus, ageing of the detectors or filter transmission in the receiver beam path on longer timescales may become an issue, and, moreover, an additional data acquisition channel will be required, adding costs to the instrument. Therefore, it was sought for alternative solutions to circumvent the speckle problem and still keep fiber-coupled detectors.

The peaks in Fig. 9 occur at timescales that are known to be typical for temperature variations caused by air conditioning. It is speculated that the very high coefficient of thermal expansion (CTE) of Spectralon is responsible for a high thermal drift. In order to test this hypothesis, we compared the behavior of the Spectralon sphere to other spheres of different materials: a commercially available gold-coated (Infragold) aluminum sphere and specifically designed gold-coated spheres with stainless steel and invar as the bulk material, respectively. The thermal expansion coefficients of the different materials used span two orders of magnitude and are listed in Table 3.

Figure 11 shows the results of this experiment. For simplicity, only a single wavelength (at 1064 nm) was used, but the Nd:YAG laser operated in double-pulse mode ($\Delta t = 360$ µs). Two 105-µm fibers were attached to two ports of the respective sphere oriented at an angle of 90° and each attached to a PIN photodiode. No special means for temperature stabilization were taken. As before, the sigma-tau plot shows the Allan

Table 3. Coefficient of Thermal Expansion (CTE) α (∼20°C) of the Bulk Material Used for the Integrating Spheres

Material	$\alpha[10^{-6}\ K^{-1}]$
Spectralon [47]	∼100–120
Aluminum	24
Steel (1.4301)	16
Invar (1.3912)	1.5

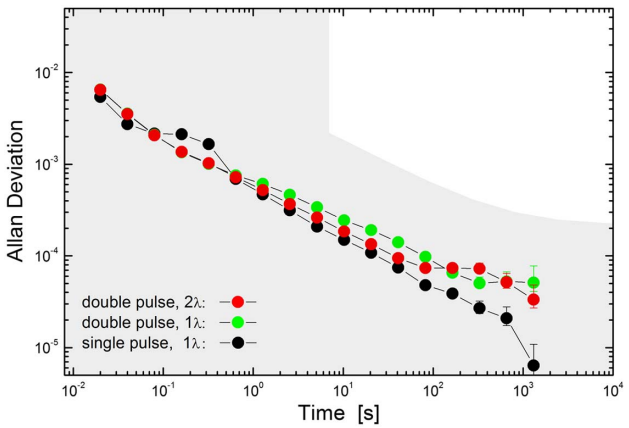

Fig. 10. Allan deviations of the DR of two subsequent pulses at 1.57 µm recorded with two pyroelectric detectors (diameter 10.5 mm). The nominal on-line/off-line double-pulse sequence is given in red and meets the A-SCOPE threshold (shaded area) and even target requirements. Green symbols designate the double-pulse mode but no switching of wavelengths, whereas the result for a single-pulse (100 Hz) sequence is given in black.

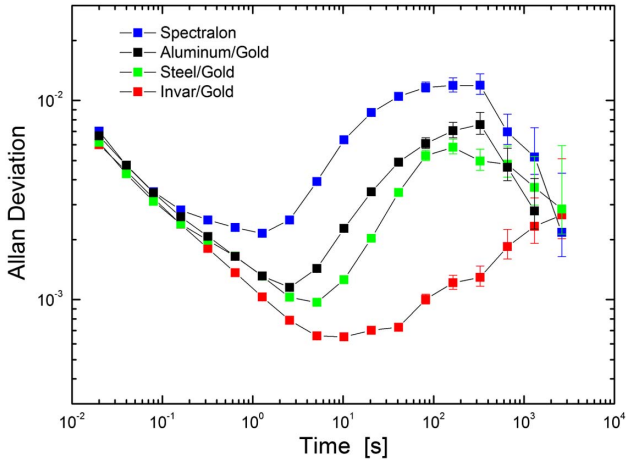

Fig. 11. Allan deviations of the DR of two subsequent pulses recorded with two fiber-coupled PIN detectors. The fiber core diameters were 105 µm. The measurements were repeated for integrating spheres with different materials (Spectralon, aluminum, stainless steel, and invar) having coefficients of thermal expansion that extend over two orders of magnitude.

deviation as a function of averaging time in a double logarithmic plot.

The shifts of the peaks towards longer averaging times approximately scale inversely with the CTE of the material used (Table 3). From this measurement series, it becomes clear that thermal behavior of the integrating sphere has a significant impact on the speckle-induced noise. Unfortunately, even the low CTE of invar does not appear to be sufficient to prevent a partial decorrelation of the speckle patterns of two individual pulses within a double-pulse sequence due to thermal expansion. In case the separation time of the pulses is much longer as for the single-pulse operation, the patterns become fully decorrelated, and thus their noise behavior is close to white.

This implies that the correlation of the two speckle patterns between two individual pulses within a double-pulse sequence is a key limitation for the measurement task. Although they found that using a PIN diode coupled to an integrating sphere yielded worse results than using a window reflection for their retrieval, other authors [33] may have overlooked this effect.

Speckles play a major (in most cases, detrimental) role in various applications requiring narrowband lasers. A variety of techniques have been investigated to reduce the speckle effect. However, many techniques cannot be applied here, such as, e.g., decreasing the coherence of the laser. For continuous-wave (cw) lasers, many techniques rely on creating some variation in the speckle pattern and averaging it over time. This may be done by vibrating the fiber (e.g., by attaching the fiber to loudspeakers [48], or PZT elements [49] by using rotating diffusors [50] or light pipes [51]. However, most speckle reduction techniques are aiming to reduce the speckle contrast only for slow detectors such as the human eye (~30 ms).

Here, we have to destroy the correlation on a time scale of ~300 μs. Several potential solutions were investigated. For example, we tried to excite the sphere and the fiber by means of, e.g., ultrasonic loudspeakers. A similar approach, but using a piezo, was employed by Ref. [52]. We could not, however, achieve significant improvement. Also, the fiber was put into an ultrasonic cleaning bath, but this did not show success. That fiber, however, had a protective jacket. Therefore, the coupling may have been unsatisfactory. Such experiments may be repeated with bare fibers in due course. These kinds of techniques are certainly not preferred options for spaceborne deployment and, therefore, were soon disregarded.

A technique that is based on speckle reduction by angular diversity provides a guideline on how to efficiently reduce the speckle effects. For this, the ends of the pick-up fibers were brought into proximity to the spheres' exit ports and mechanically vibrated. This was realized by cleaving the fibers (200-μm core diameter) and attaching their ends close to the eccentric of a miniature vibration motor typically used for mobile phones (Copal LA4-432A). This motor has a rated speed of 9500 rpm, and the fiber end was protruded, such that the stroke was a few millimeters giving rise to a sufficiently high displacement of more than the size of an individual speckle [Eq. (12)] within the pulse separation time of 360 μs. Therefore, the speckle pattern should be decorrelated. Apart from this, the setup otherwise corresponds to the one described above.

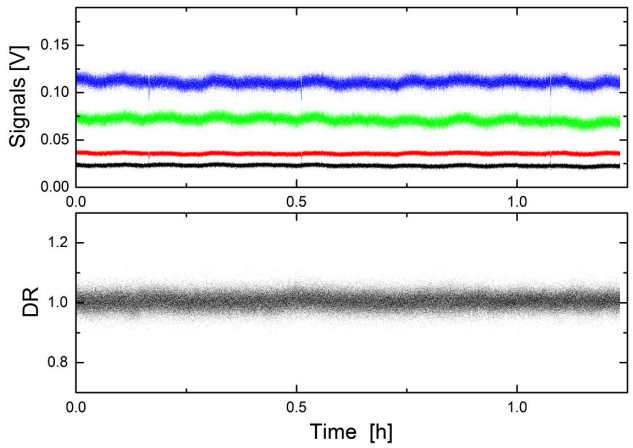

Fig. 12. Time series of the individual detector signals (top) and the respective DR (bottom), analogous to Fig. 8, over 1.2 h of operation. The InGaAs photodiodes were fiber coupled using multimode fibers with a core diameter of 200 μm and mechanically vibrated.

Indeed, the vibrating fibers lead to the desired effect, and the signals of the detectors and the DR over a time series of 1.2 h are depicted in Fig. 12. The DR significantly differs from the behavior shown in Fig. 8 and appears to be statistically distributed around its target value of 1.

The Allan analysis depicted in Fig. 13 shows a more quantitative result. Indeed, the Allan deviation of the DR closely follows a −1/2-behavior. In this Figure, the Allan deviation is shown for the case without countermeasures (motors off) and with rotating motors. The OPO was operated in double-pulse mode and either at the on-line wavelength only or in the nominal on–off scheme. It is clearly seen that the noise increases significantly (by about one order of magnitude) for

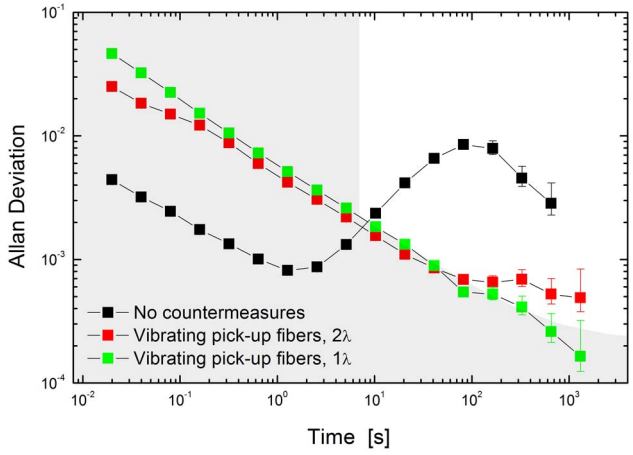

Fig. 13. Allan deviations of the DR of two subsequent pulses in double-pulse operation of the OPO at 1.57 μm recorded with two fiber-coupled PIN detectors with a fiber diameter of 200 μm. The black symbols show the result with no speckle reduction measures applied, and the red and green symbols show the result with the vibrating fibers in single- and dual-wavelength operation, respectively. The shaded area depicts the range for the A-SCOPE threshold requirements.

the short averaging times, but follows white-noise behavior in contrast to the non-vibrating fiber, which shows a distinct enhancement of noise at averaging times of ~100 s. The amplitude of the vibration should be large enough to capture an entirely different speckle pattern for the two pulses in the double-pulse sequence. The difference between single- and dual-wavelength operation is only marginal.

Unfortunately, this solution appears not to be an option for either spaceborne or airborne deployment due to limited operational lifetime of the motor and also of the fiber due to abrasion from the motor's eccentric. However, on the basis of the findings, a setup was realized, implemented, and tested using the CHARM-F lidar system in airborne operation.

6. AIRBORNE ENERGY MONITORING SUB-MODULE

A. Design

A possible alternative solution to the vibrating fibers that uses angular diversity consists of destroying the speckle patterns by using rotating diffusors. An alternative way that gets around moving mechanics is the use of electroactive polymers (EAP) [53]. Such devices, which are, e.g., used in laser projection or microscopy, have become commercially available (Optotune, Switzerland). Their advantage is their compactness and light weight; they are vibration free, require only low electrical power (USB), operate in a wide temperature range (−30°C – 85°C), and are insensitive to shock. Disadvantages are that they are limited in aperture to currently ~10 mm, and their polymer membrane cannot be anti-reflection (AR) coated. We used devices with appropriate AR coatings (1100–1700 nm) on the cover glasses. Their yet specified lifetime of ~6000 h is acceptable for airborne operation but not for a satellite mission lifetime of three years.

Due to the advantageous properties of a double sphere layout concerning attenuation, we designed a setup consisting of two Spectralon spheres with an EAP diffuser in between. In the lab, tests were performed that confirmed that the speckle reduction behavior was comparable to the vibrating fiber approach and was therefore chosen for the CHARM-F system.

Furthermore, a pick-up device is required to inject a tiny portion of the outgoing laser beam for energy calibration. One of the easiest and most straightforward solutions that promises negligible wavelength dependence is an optical wedge beam splitter (WBS), which consists of a prism of transparent material with a small apex angle. The theory of the wedged beam splitter has been developed by Ref. [54]. Optimally, the wedge should be made out of a stable material such as fused silica. Here, however, we decided to use a diffractive optical element (DOE) to facilitate integration based on design-engineering aspects.

Diffractive beam samplers are typically used to monitor high-power lasers where optical losses and wavefront distortions of the transmitted beam need to be kept to a minimum. In most applications, most of the incident light must continue forward, "unaffected," in the "zero order," while a small amount of the beam is diffracted into a higher order, providing a "sample" of the beam. Placing this diffractive optical element directly in front of the integrating sphere enables to sample the +1 order and −1 order while transmitting its zero order into the atmosphere. The DOEs used within this study were custom designed by Holo/Or Ltd., Israel, with fused silica used as the etching substrate. They have a diameter of 1″, a thickness of 3 mm, and are equipped with a broadband antireflection coating that covers wavelength between 1500 nm and 1650 nm. The sampling ratio is specified to be 0.25%; thus, only a negligible part of the outgoing light is used for the energy monitoring.

During test experiments performed using a double-pulse, two-wavelength mode of the OPO both solutions, WBS and DOE, performed nearly identically over time series of >2 h and did not deteriorate the noise performance. Thus, both appear to be viable solutions.

In summary, based on our laboratory investigations, two energy-monitoring sub-modules were built for both the CH_4 and CO_2 channels of CHARM-F according to the design schematically shown in Fig. 14. It combines the four important aspects: (1) pick-up, (2) speckle reduction, (3) attenuation, and (4) routing to detector.

As the pick-up device, a DOE was used. The zero diffraction order passes the first Spectralon sphere and is transmitted into the atmosphere, while the +1 and −1 orders are injected into the sphere that has a diameter of 3.3". The second Spectralon sphere has a diameter of 1.5" and provides two fiber ports from where the sampled light is guided to the detectors using appropriate fibers. In between both spheres, the polymer diffuser is placed. By selection of the hole diameter between the spheres, the attenuation can be adapted to the levels required (Fig. 14). The fibers were guided to their respective detector units (Fig. 15), i.e., to the 200-µm avalanche photodiode (APD) and to the 1-mm quadrant PIN. In the preliminary design, a 100-m-long fiber with a core size of 200 µm and a

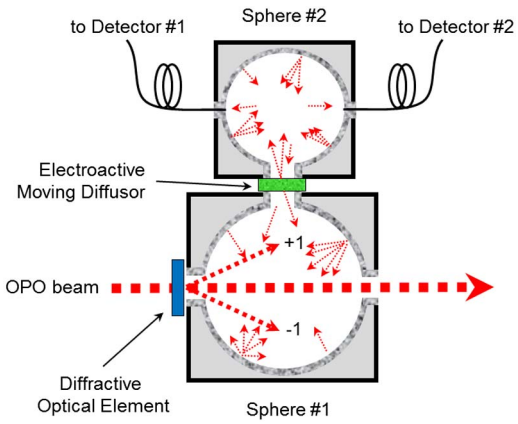

Fig. 14. Schematic setup of the energy-monitoring sub-module. Part of the incoming beam is diffracted into the first sphere using a diffractive optical element. Between the first and second spheres, the electroactive diffusor serves to reduce the speckle-related noise. By means of changing the size of the hole between the two spheres, the overall attenuation can be adapted. The attenuated signals are picked up using two fibers attached to the port of sphere #2. Two such modules are synchronously used for the CO_2 and CH_4 channels of CHARM-F, respectively. For simplicity, the ports are schematically depicted in two dimensions. In reality, they are oriented in three dimensions with respect to the incoming beam.

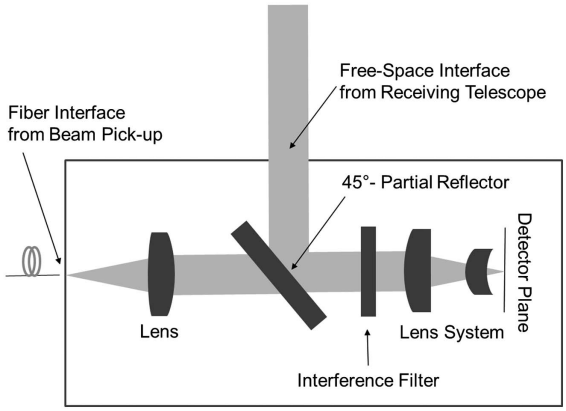

Fig. 15. Schematic of CHARM-F's detector setup. The beams from the pick-up (for energy calibration) and from the ground return are overlapped using a partial reflector. A lens system images the fiber end onto the detector. The general layout is the same for all four detector units.

NA of 0.39 was used for the APD, and a 4-m-long fiber with a core diameter of 400 μm and NA of 0.39 was used for the PIN diode in the CO_2 channel. For the CH_4 channel, the fibers for the APD (PIN) had a length of 100 m (30 m), a diameter of 200 μm (550 μm), and NA of 0.39 (0.22), respectively. These fibers were chosen for reasons of availability. After the experiments described below, both channels were finally equipped with optimized fibers (CeramOptec) having a diameter of 200 μm (APD) and 600 μm (PIN). All fibers are 100 m long to enable a decent temporal separation between outgoing and reference pulses and have a large NA = 0.48.

B. Airborne Tests

CHARM-F is designed as an airborne demonstrator for spaceborne greenhouse lidar missions, in particular the French–German satellite mission MERLIN [18]. However, CHARM-F does not measure CH_4, only, but is able to measure both most important anthropogenic GHGs, CO_2 and CH_4, at the same time. For this purpose, the entire system consists of two independent lidar transmitters at wavelengths of ∼1645 nm (appropriate for CH_4) and at ∼1572 nm (appropriate for CO_2). The two transmitter parts share only a reference cell, system control, and data acquisition computers. The transmitter architecture is very close to the test bed used for the laboratory experiments described above. The respective wavelengths are generated by OPOs that are pumped by injection-seeded, double-pulse Nd:YAG lasers in a master-oscillator-power-amplifier configuration at a repetition frequency of 50 Hz. The OPOs are injection seeded using DFB lasers. In order to exactly lock the seed lasers to the required on- and off-line frequencies, a reference cell filled with both CO_2 and CH_4 is used. Two master DFB lasers are transmitted through the cell and locked to respective absorption lines of the two gases using wavelength modulation. The on-line seed lasers are stabilized with respect to their masters using an offset-locking technique. The OPO cavities are matched to the on-line wavelengths using the same heterodyne technique as described in Section 4.A. Also, the stabilization of the off-line seed lasers uses the same method. For further information about the CHARM-F system, the reader is referred to Ref. [15].

The receiving system of CHARM-F features unique properties that proved to be advantageous for the performance test of the energy calibration. The return signal for each wavelength is not recorded by a single telescope, but by two telescopes. Thus, four telescopes are employed in total. Each trace gas channel has a small (60-mm) telescope with an avalanche InGaAs APD (200-μm-diameter) as the detector plus a larger (200-mm) telescope with a quadrant InGaAs PIN diode (1-mm-diameter), respectively. The original motivation for designing this sophisticated receiving system was that the large telescope appears to be optimum for airborne use, while the small telescope mimics the geometry of a spaceborne instrument. Using these two channels, the on-line/off-line ratio can be compared in flight by means of two independent detectors with the same statistical method as described above, which is a significant asset.

The flight campaign was successfully performed onboard the German research aircraft HALO in spring 2015. The general purpose of this campaign was, on the one hand, the finalization of the airworthiness certification of CHARM-F and, on the other hand, the testing of the overall behavior of the sub-systems, including the energy-monitoring device during flight conditions and collection of first scientific measurement data. During the campaign, five flights with about 22 flight hours in total took place mostly in German, Italian, and Polish airspace. Details have been published in Ref. [15].

Concerning evaluation of the energy-monitoring device, data from three different flights on 5, 11, and 13 May 2015 were selected, which provide sufficient long flight legs that are not too much influenced by near cirrus clouds and that do not include too many parameter changes requested by the technical flight program. For the Allan evaluation, we therefore have to

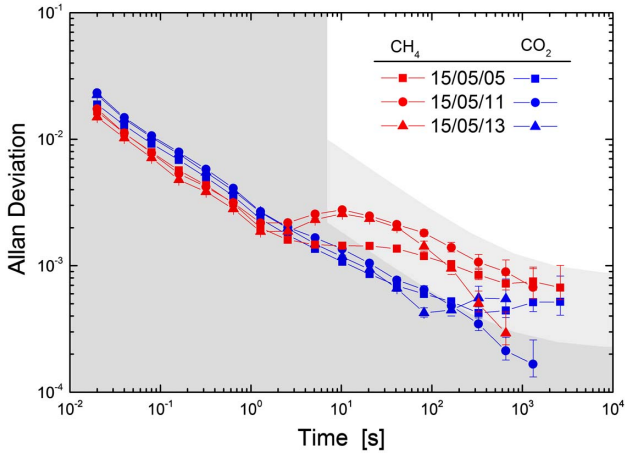

Fig. 16. Allan deviations of the energy ratio recorded during three different flights on 5, 11, and 13 May 2015. The OPOs were nominally operated in 2 – λ, double-pulse operation at the CO_2 and CH_4 wavelengths at ∼1572 nm and 1645 nm, respectively. The on–off energy ratios were independently measured using the two different receiving channels. The shaded areas depict the range of the threshold requirements defined for this project (CH_4, light gray; CO_2, dark gray).

make a few concessions, in that the time series used does not consist of an uninterrupted series of points. However, this is not expected to alter the Allan variance significantly. Figure 16 shows the evaluated Allan deviation of the energy ratio for these three flights for both CO_2 and CH_4 channels. Although from different days and different flights, all curves are similar and close to a slope $-1/2$, indeed, there is some minor deviation noticeable for the CH_4 case at time scales between 10 s and 100 s. The reason is not clear but could be due to the different pick-up fibers used or a different thermal regime, since the CH_4 channel is located farther away from the aircraft window. However, and most important, the threshold requirements for the two greenhouse gases are mostly met.

7. CONCLUSIONS AND OUTLOOK

Accurate calibration of the pulse energy of narrowband lasers is a challenging task that is of particular importance for IPDA measurements of GHGs from air and space. Meeting the stringent requirements for monitoring of CO_2 or CH_4 using this technique requires the ratio of outgoing on- and off-line pulses to be determined to high accuracies. Based on our allocation of individual contributions to the overall error budget, accuracies on the order of less than $2.2 \cdot 10^4$ are requested for CO_2 (and ~3–4 times higher for CH_4), unless independent means for correcting for residual offsets or trends can be applied.

In order to assess the requirements on different time scales involved and address both statistical and systematic errors, an innovative evaluation scheme based on the Allan variance was introduced. By means of that scheme, different energy calibration schemes were investigated.

In order to provide negligible dependence of beam profile and beam pointing, integrating spheres show much promise as part of an energy calibration device. However, integrating spheres produce speckle effects and, as in hard-target lidar returns [55–57], they play an important role also for the energy referencing due to the coherence of the lidar transmitter. In order to reduce the speckle noise to acceptable levels, two options have been investigated. The first one uses direct coupling of a large (pyroelectric) detector to the integrating sphere. Such detectors are fast enough to separate the outgoing on- and off-line double pulses, which are separated by a few hundreds of microseconds, while also providing a detection area large enough to capture so many speckles that the effective noise is reduced to acceptable levels. Using such a setup, the resulting noise exhibited pure white noise behavior with a noise level easily meeting even the stringent target requirements for a spaceborne CO_2 IPDA such as A-SCOPE.

Despite a superior performance with respect to its precision for the energy ratio monitoring, this method exhibits a potential disadvantage. It requires a separate detector acting as the energy monitor. Since ageing effects of detectors, interference filters, or coatings in the receiving light path that act differently for the two wavelengths may lead to varying biases, it seems advisable to use a single detection path for both return signal and energy monitor. This requires highly sensitive optical semiconductor detectors that generally have a small aperture, and thus are prone to speckle effects. At the same time, the monitor energy has to be reduced by several orders of magnitude to match the light level of the lidar returns. As demonstrated, that task can be performed by means of single- or double-integrated spheres with fiber coupling. Such a simple setup, however, was found to be inadequate to meet the stringent requirements due to speckle noise. Therefore, means for speckle noise reduction have to be implemented. The reason for increased speckle noise was identified to be a partial correlation of the speckle patterns for two pulses within a double-pulse sequence. While a larger temporal separation leads to a sufficient decorrelation, this is not an option for the measurement task, since it requires both pulses to be emitted as close as possible to provide a good overlap match on the target. Therefore, it was attempted to decorrelate the speckle patterns by creating some variation and averaging it over time. A successful implementation was realized by using an electroactive polymer diffusor in between two integrating spheres. This method, although increasing the noise on short timescales, led to almost white-noise behavior and significantly reduced the speckle noise on the more relevant longer timescales, such that the overall noise criteria could be fulfilled.

On the basis of the experimental findings, a calibration chain was devised for the airborne CO_2 and CH_4 IPDA CHARM-F, which did meet the requirements under in-flight conditions. Although adequate for airborne applications, the guaranteed lifetime of the electroactive polymer diffusors is not acceptable for a spaceborne lidar due to degradation of the polymers. Nevertheless, a next generation of speckle reducers based on reluctance force-based oscillating diffusors shows much promise also for long-term operation [58]. Using such novel capabilities and better adapted fiber design, the calibration chain of CHARM-F will continuously be improved for its upcoming deployments.

At the same time, the findings of the current study give important guidelines for the design of upcoming spaceborne GHG IPDA missions such as MERLIN. However, this study is deemed important not only for lidars but for energy calibration measurements in general.

Funding. European Space Agency (ESA) (4000106330/12/NL/EM); Bundesministerium für Wirtschaft und Technologie (BMWi) (FKZ 50 EP 1001) within the MERLIN mission on behalf of DLR Space Administration.

Acknowledgment. We would like to thank Hamid R. Khalesifard and Marco Miebach for experimentally supporting the energy monitoring experiments. We appreciate helpful discussions with David Epner from Epner Technology, Inc., concerning gold coatings on rough surfaces.

REFERENCES

1. G. Ehret, C. Kiemle, M. Wirth, A. Amediek, A. Fix, and S. Houweling, "Space-borne remote sensing of CO_2, CH_4, and N_2O by integrated path differential absorption lidar: a sensitivity analysis," Appl. Phys. B **90**, 593–608 (2008).
2. WMO World Data Centre for Greenhouse Gases, "WDCGG data summary No. 41," 2017.
3. A. Amediek, A. Fix, M. Wirth, and G. Ehret, "Development of an OPO system at 1.57 μm for integrated path DIAL measurement of atmospheric carbon dioxide," Appl. Phys. B **92**, 295–302 (2008).
4. D. Sakaizawa, S. Kawakami, M. Nakajima, Y. Sawa, and H. Matsueda, "Ground-based demonstration of a CO_2 remote sensor

using a 1.57 μm differential laser absorption spectrometer with direct detection," J. Appl. Remote Sens. **4**, 043548 (2010).
5. J. B. Abshire, H. Riris, G. R. Allan, C. J. Weaver, J. Mao, X. Sun, W. E. Hasselbrack, S. R. Kawa, and S. Biraud, "Pulsed airborne lidar measurements of atmospheric CO_2 column absorption," Tellus **62**, 770–783 (2010).
6. G. D. Spiers, R. T. Menzies, J. Jacob, L. E. Christensen, M. W. Phillips, Y. Choi, and E. V. Browell, "Atmospheric CO_2 measurements with a 2 μm airborne laser absorption spectrometer employing coherent detection," Appl. Opt. **50**, 2098–2111 (2011).
7. H. Riris, K. Numata, S. Li, S. Wu, A. Ramanathan, M. Dawsey, J. Mao, R. Kawa, and J. B. Abshire, "Airborne measurements of atmospheric methane column abundance using a pulsed integrated-path differential absorption lidar," Appl. Opt. **51**, 8296–8305 (2012).
8. D. Sakaizawa, S. Kawakami, M. Nakajima, T. Tanaka, I. Morino, and O. Uchino, "An airborne amplitude-modulated 1.57 μm differential laser absorption spectrometer: simultaneous measurement of partial column- averaged dry air mixing ratio of CO_2 and target range," Atmos. Meas. Tech. **6**, 387–396 (2013).
9. J. Dobler, F. Harrison, E. Browell, B. Lin, D. McGregor, S. Kooi, Y. Choi, and S. Ismail, "Atmospheric CO_2 column measurements with an airborne intensity-modulated continuous-wave 1.57-μm fiber laser lidar," Appl. Opt. **52**, 2874–2892 (2013).
10. J. B. Abshire, A. Ramanathan, H. Riris, J. Mao, G. R. Allan, W. E. Hasselbrack, C. J. Weaver, and E. V. Browell, "Airborne measurements of CO_2 column concentration and range using a pulsed direct detection IPDA lidar," Remote Sens. **6**, 443–469 (2014).
11. R. T. Menzies, G. D. Spiers, and J. C. Jacob, "Airborne laser absorption spectrometer measurements of atmospheric CO_2 column mole fractions: source and sink detection and environmental impacts on retrievals," J. Atmos. Ocean. Technol. **31**, 404–421 (2014).
12. F. Gibert, D. Edouart, C. Cenac, and F. Le Mounier, "2-μm high-power multiple-frequency single-mode Q-switched Ho:YLF laser for DIAL application," Appl. Phys. B **116**, 967–976 (2014).
13. J. Yu, M. Petros, U. Singh, T. Refaat, K. Reithmaier, R. Remus, and W. Johnson, "An airborne 2-μm double-pulsed direct-detection lidar instrument for atmospheric CO_2 column measurements," J. Atmos. Ocean. Technol. **34**, 385–400 (2017).
14. J. Du, Y. Sun, D. Chen, Y. Mu, M. Huang, Z. Yang, J. Liu, D. Bi, X. Hou, and W. Chen, "Frequency-stabilized laser system at 1572 nm for space-borne CO_2 detection LIDAR," Chin. Opt. Lett. **15**, 031401 (2017).
15. A. Amediek, G. Ehret, A. Fix, M. Wirth, C. Büdenbender, M. Quatrevalet, C. Kiemle, and C. Gerbig, "CHARM-F—a new airborne integrated-path differential-absorption lidar for carbon dioxide and methane observations: measurement performance and quantification of strong point source emissions," Appl. Opt. **56**, 5182–5197 (2017).
16. ESA, "A-SCOPE—Advanced space carbon and climate observation of planet earth," Report for Assessment, SP-1313/1 (ESA-ESTEC, 2008).
17. NASA, "ASCENDS mission science definition and planning workshop report," 2008, https://cce.nasa.gov/ascends.
18. G. Ehret, P. Bousquet, C. Pierangelo, M. Alpers, B. Millet, J. B. Abshire, H. Bovensmann, J. P. Burrows, F. Chevallier, P. Ciais, C. Crevoisier, A. Fix, P. Flamant, C. Frankenberg, F. Gibert, B. Heim, M. Heimann, S. Houweling, H. W. Hubberten, P. Jöckel, K. Law, A. Löw, J. Marshall, A. Agusti-Panareda, S. Payan, C. Prigent, P. Rairoux, T. Sachs, M. Scholze, and M. Wirth, "MERLIN: a French-German space lidar mission dedicated to atmospheric methane," Remote Sens. **9**, 1052 (2017).
19. R. T. Menzies and D. M. Tratt, "Differential laser absorption spectrometry for global profiling of tropospheric carbon dioxide: selection of optimum sounding frequencies for high precision measurements," Appl. Opt. **42**, 6569–6577 (2003).
20. J. Caron and Y. Durand, "Operating wavelengths optimization for a spaceborne lidar measuring atmospheric CO_2," Appl. Opt. **48**, 5413–5422 (2009).
21. W. J. Riley, *Handbook of Frequency Stability Analysis*, NIST Special Publication 1065 (National Institute of Standards and Technology, 2008).
22. S. R. Gunn, "Calorimetric measurements of laser energy and power," J. Phys. E **6**, 105–114 (1973).
23. S. B. Lang, "Pyroelectricity: from ancient curiosity to modern imaging tool," Phys. Today **58**(8), 31–36 (2005).
24. D. J. Livigni, *High-Accuracy Laser Power and Energy Meter Calibration Service*, NIST Special Publication 250-62 (National Institute of Standards and Technology, 2003).
25. I. Vayshenker, H. Haars, X. Li, J. H. Lehman, and D. J. Livigni, "Comparison of optical-power meters between the NIST and the PTB," Metrologia **37**, 349–350 (2000).
26. D. Fukuda, S. Kimura, and M. Endo, "Absolute energy reference calorimeter with bismuth telluride thermocouples for laser energy standard," Rev. Sci. Instrum. **76**, 113107 (2005).
27. M. G. White, R. Leonhardt, D. Livigni, and J. H. Lehman, "A CW calibrated laser pulse energy meter for the range 1 pJ to 100 mJ," Metrologia **51**, 225–234 (2014).
28. E. R. Murray, J. E. van der Laan, and J. G. Hawley, "Remote measurement of HCl, CH_4, and N_2O using a single-ended chemical-laser lidar system," Appl. Opt. **15**, 3140–3148 (1976).
29. E. R. Murray and J. E. van der Laan, "Remote measurement of ethylene using a CO_2 differential-absorption lidar," Appl. Opt. **17**, 814–817 (1978).
30. A. P. Force, D. K. Killinger, W. E. DeFeo, and N. Menyuk, "Laser remote sensing of atmospheric ammonia using a CO_2 lidar system," Appl. Opt. **24**, 2837–2841 (1985).
31. R. A. Baumgartner and R. L. Byer, "Continuously tunable IR lidar with applications to remote measurements of SO_2 and CH_4," Appl. Opt. **17**, 3555–3561 (1978).
32. M. Queißer, M. Burton, and L. Fiorani, "Differential absorption lidar for volcanic CO_2 sensing tested in an unstable atmosphere," Opt. Express **23**, 6634–6644 (2015).
33. T. Refaat, U. Singh, M. Petros, R. Remus, and J. Yu, "Self-calibration and laser energy monitor validations for a double-pulsed 2-μm CO_2 integrated path differential absorption lidar application," Appl. Opt. **54**, 7240–7251 (2015).
34. K. Numata, S. Wu, and H. Riris, "Fast-switching methane lidar transmitter based on a seeded optical parametric oscillator," Appl. Phys. B **116**, 959–966 (2014).
35. M. Quatrevalet, X. Ai, A. Pérez-Serrano, P. Adamiec, J. Barbero, A. Fix, J. M. G. Tijero, I. Esquivias, J. G. Rarity, and G. Ehret, "Atmospheric CO_2 sensing with a random modulation continuous wave integrated path differential absorption lidar," IEEE J. Sel. Top. Quantum Electron. **23**, 157–167 (2017).
36. K. Carr, "Integrating sphere theory and applications. Part I: Integrating sphere theory and design," Surf. Coat. Int. **80**, 380–385 (1997).
37. C. J. Bruegge, A. E. Stiegman, R. A. Rainen, and A. W. Springsteen, "Use of spectralon as a diffuse reflectance standard for in-flight calibration of earth-orbiting sensors," Opt. Eng. **32**, 805–814 (1993).
38. J. W. Pickering, C. J. M. Moes, H. J. C. M. Sterenborg, S. A. Prahl, and M. J. C. van Gemert, "Two integrating spheres with an intervening scattering sample," J. Opt. Soc. Am. A **9**, 621–631 (1992).
39. G. D. Boreman, A. B. Centore, and Y. Sun, "Generation of laser speckle with an integrating sphere," Opt. Eng. **29**, 339–342 (1990).
40. J. C. Dainty, "The statistics of speckle patterns," in *Progress in Optics XIV*, E. Wolf, ed. (North Holland, 1976).
41. D. Masiyano, J. Hodgkinson, and R. P. Tatam, "Gas cells for tunable diode laser absorption spectroscopy employing optical diffusers. Part 2: Integrating spheres," Appl. Phys. B **100**, 303–312 (2010).
42. J. W. Goodman, *Speckle Phenomena in Optics: Theory and Applications* (Roberts & Company, 2007).
43. S. C. McClain, C. L. Bartlett, J. L. Pezzaniti, and R. A. Chipman, "Depolarization measurements of an integrating sphere," Appl. Opt. **34**, 152–154 (1995).
44. A. Fix, C. Büdenbender, M. Wirth, M. Quatrevalet, A. Amediek, C. Kiemle, and G. Ehret, "Optical parametric oscillators and amplifiers for airborne and spaceborne active remote sensing of CO_2 and CH_4," Proc. SPIE **8182**, 818206 (2011).
45. J. W. Goodman, "Statistical properties of laser speckle patterns," in *Laser Speckle and Related Phenomena*, J. C. Dainty, ed., 2nd ed. (Springer-Verlag, 1984).

46. G. Parry, "Some effects of surface roughness on the appearance of speckle in polychromatic light," Opt. Commun. **12**, 75–78 (1974).
47. Labsphere Technical Guide, "A guide to reflectance coatings and materials," https://www.labsphere.com.
48. B. Daino, G. De Marchis, and S. Piazzolla, "Speckle and modal noise in optical fibres: theory and experiment," J. Mod. Opt. **27**, 1151–1159 (1980).
49. W.-S. Ha, S.-J. Lee, K.-H. Oh, Y.-M. Jung, and J.-K. Kim, "Speckle reduction in near-field image of multimode fiber with a piezoelectric transducer," J. Opt. Soc. Korea **12**, 126–130 (2008).
50. S. Lowenthal and D. Joyeux, "Speckle removal by a slowly moving diffuser associated with a motionless diffuser," J. Opt. Soc. Am. A **61**, 847–851 (1971).
51. M. Sun and Z. Lu, "Speckle suppression with a rotating light pipe," Opt. Eng. **49**, 024202 (2010).
52. S. Potvin and J. Genest, "Reducing the effect of integrating sphere speckle when characterizing the instrument line shape of a Fourier-transform hyperspectral imager," Appl. Opt. **48**, 5849–5852 (2009).
53. C. Graetzel, M. Suter, and M. Aschwanden, "Reducing laser speckle with electroactive polymer actuators," Proc. SPIE **9430**, 943004 (2015).
54. Y. Beers, *The Theory of the Optical Wedge Beam Splitter*, NBS Monograph 146 (National Bureau of Standards, 1974).
55. E. P. MacKerrow, M. J. Schmitt, and D. C. Thompson, "Effect of speckle on lidar pulse-pair ratio statistics," Appl. Opt. **36**, 8650–8669 (1997).
56. E. P. MacKerrow and M. J. Schmitt, "Measurement of integrated speckle statistics for CO_2 lidar returns from a moving, nonuniform, hard target," Appl. Opt. **36**, 6921–6937 (1997).
57. G. A. Wagner and D. F. Plusquellic, "Ground-based, integrated path differential absorption LIDAR measurement of CO_2, CH_4, and H_2O near 1.6 μm," Appl. Opt. **55**, 6292–6310 (2016).
58. D. Stadler, M. Suter, M. Ventura, and D. Niederer, "Speckle reduction with reluctance force-based oscillating diffusors," in *4th Laser Display and Lighting Conference (LDC)* (2015).